Kajikawa et al. Progress in Earth and Planetary Science (2016) 3:16
DOI 10.1186/s40645-016-0094-5

Progress in Earth and Planetary Science

RESEARCH ARTICLE Open Access

Resolution dependence of deep convections in a global simulation from over 10-kilometer to sub-kilometer grid spacing

Yoshiyuki Kajikawa[1*], Yoshiaki Miyamoto[1], Ryuji Yoshida[1], Tsuyoshi Yamaura[1], Hisashi Yashiro[1] and Hirofumi Tomita[1,2]

Abstract

The success of sub-kilometer global atmospheric simulation opens the door for resolving deep convections, which are fundamental elements of cloudy disturbances that drive global circulation. A previous study found that the essential change in the simulated convection properties occurred at a grid spacing of about 2 km as a global mean. In grid-refinement experiments, we conducted further comprehensive analysis of the global-mean state and the characteristics of deep convection, to clarify the difference of the essential change by location and environment. We found that the essential change in convection properties was different in the location and environment for each cloudy disturbance. The convections over the tropics show larger resolution dependence than convections over mid-latitudes, whereas no significant difference was found in convections over land or ocean. Furthermore, convections over cloudy disturbances [(i.e., Madden-Julian oscillation (MJO), tropical cyclones (TCs)] show essential change of convection properties at about 1 km grid spacing, suggesting resolution dependence. As a result, convections not categorized as cloudy disturbances make a large contribution to the global-mean convection properties. This implies that convections in disturbances are largely affected organization processes and hence have more horizontal resolution dependence. In contrast, other categorized convections that are not involved in major cloudy disturbances show the essential change at about 2 km grid spacing. This affects the latitude difference of the resolution dependence of convection properties and hence the zonal-mean outgoing longwave radiation (OLR). Despite the diversity of convection properties, most convections are resolved at less than 1 km grid spacing. In the future, longer integration of global atmosphere, to 0.87 km grid spacing, will stimulate significant discussion about the interaction between the convections and cloudy disturbances.

Keywords: Deep convection, High resolution, Global simulation, NICAM, Cloudy disturbance, Resolution dependence

Background

The rapid increase of computer capabilities has enabled meteorological and climatological researchers to increase horizontal and vertical resolutions in the numerical model (Simmons et al. 1989; Mizuta et al. 2006; Saito et al. 2006; Kodama et al. 2015). The demand for high-resolution simulation not only from regional-model researchers but also from global-model researchers has become intense. In the atmospheric general circulation model (AGCM), one of the key issues is to explicitly resolve deep convection for the following reasons.

Deep convection is a minimum element for the organization of cloud systems, including cloudy disturbances, and plays an essential role in driving the atmosphere, through the transportation of energy in the troposphere from the tropics to the polar region (Webster 1972; Gill 1982; Emanuel and Raymond 1993). Cloudy disturbances are sometimes associated with natural disasters

* Correspondence: ykaji@riken.jp
[1]RIKEN Advanced Institute for Computational Science, 7-1-26 Minatojima-minami-machi, Chuo-ku, Kobe, Hyogo 650-0047, Japan
Full list of author information is available at the end of the article

because of related heavy rainfall; hence, it is important to enrich our understanding of the processes and mechanisms of cloudy disturbances. One of the important processes that characterize cloudy disturbances is the interaction between deep convection and cloudy disturbances through the hierarchical structure of cloud cluster and super cloud cluster (SCC). SCC is the eastward-moving convection area near the equator with a horizontal scale of 2000–4000 km (Nakazawa 1988; Mapes and Houze 1993). However, it has been difficult to obtain observational data that is spatiotemporal enough to examine that process (Stephens et al. 2010; Mrowiec et al. 2012). Numerical simulations have been used to compensate the deficiency and gaps in observational data. The ability to express deep convection, with its effect on larger-scale phenomenon, is crucial for better simulating global circulation and associated organizations of cloud systems and disturbances.

However, because there is a large gap in spatiotemporal scale between convection on the order of 10^0–10^1 km and cloudy disturbances on the order of 10^3 km, it has been challenging to globally simulate both phenomena and comprehensively discuss their interaction. In previous decades, due to the low horizontal resolution of the model, clouds have been expressed as parameterization. Various types of cumulus parameterization were established and have been used in the AGCM [e.g., (Arakawa and Schubert 1974; Kain and Fritsch 1990; Yoshimura et al. 2015)]. The variety of these parameterizations has been a source of uncertainties in model results.

It is impossible for a conventional GCM to represent the hierarchy of cloud organization from elemental convective clouds. Thus, comprehensive understanding, including the impact of organized clouds on general circulation, was not realistic. The new Nonhydrostatic Icosahedral Atmospheric Model (NICAM) (Tomita and Satoh 2004; Satoh et al. 2008; Satoh et al. 2014) is designed to conduct global simulation without cumulus parameterization. Previous studies have shown the usefulness of the global nonhydrostatic model without cumulus parameterization for large-scale organized convective systems and disturbances, such as tropical cyclones (Fudeyasu et al. 2008; Yamaura et al. 2013; Miyamoto et al. 2014; Nakano et al. 2015), the Madden-Julian oscillation (MJO) (Miura et al. 2007; Miyakawa et al. 2014), and monsoon onset (Kajikawa et al. 2015). However, in the early 2010s, the horizontal grid spacing with 3.5 km was limited. Although this resolution was the best possible in those days for qualitatively acceptable results for the cloud disturbance expression, the impact of higher resolution on model results was expected for the interaction between different spatiotemporal scale phenomena.

Because of these considerations, Miyamoto et al. (2013) (hereafter MY13) successfully conducted the first-ever global atmosphere simulations with sub-kilometer grid spacing. They further stepped forward to resolve the convection for the entire Earth. Through a set of grid-refinement experiments from over 10 km to sub-kilometer, they found that the simulated convection core averaging over the globe is expressed not by a single grid point but by multiple grid points in the sub-kilometer grid-spacing simulation. They also showed that the expression of convection core was drastically changed between 3.5 and 1.7 km grid spacing. Furthermore, Miyamoto et al. (2015) (hereafter MY15) conducted detailed analysis for convections simulated in the finest grid spacing. They explained that the statistical properties of deep convection are significantly different in various cloudy disturbances, such as MJOs or tropical cyclones (TCs).

In short, we have been in a transition stage of improving the representation of cloud processes, including the feedbacks, with computer resources (Randall et al. 2003), and deep convection is one of the important components of climate modeling (Stevens and Bony 2013). The success of sub-kilometer global atmospheric simulation in MY13 and MY15 opens the door to the next stage of global research for deep convection and the cloudy disturbances that arise from its organization, by truly resolving the deep convection.

However, several issues remain. The primary issue is the dependence of the essential change of convection properties on the location and environment of the grid spacing under consideration. MY13 showed the change in the sense of global mean and the subsequent paper, and MY15 clarified the different convection aspects between the main cloud disturbances under the highest resolution simulation only. MY13 did not discuss the dependence on the cloud disturbance, while MY15 did not discuss the dependence on the resolution. In this study, we investigate the primary issue more comprehensively, considering both MY13 and MY15. The specific question is as follows: In what area does convection make the larger contribution to the resolution dependence of detected convection properties averaging over the globe as shown in MY13? Another important question is as follows: What environmental condition is effective in producing the diversity of convection properties, i.e., what is the resolution relationship between the number of deep convections, areas of deep convection, vertical mass flux outgoing longwave radiation (OLR), and precipitation? In this paper, we perform comprehensive analysis to address these questions and resolve the issues by describing an overview of sub-kilometer global simulation with a set of grid-refinement experiments.

Methods

We used a set of global atmospheric simulation results of a grid-refinement experiment. The simulation was conducted using NICAM. The number of vertical layers was 94, and the grid interval gradually expanded with height. The height of the lowest level was 36 m, and the average resolutions in the boundary layer and in the troposphere were about 80 and 250 m, respectively. The height of the top of the atmosphere was 39,291 m. The detailed description of the dynamical core is summarized in Tomita and Satoh (2004). Physical processes such as radiation process, microphysical process, boundary-layer turbulence, and surface flux were solved using the parameterizations of Sekiguchi and Nakajima (2008), Tomita (2008), Noda et al. (2010), and Louis (1979). Cumulus parameterization was not used in any experiment. The horizontal grid spacing in the series of experiments was set at 0.87, 1.7, 3.5, 7.0, and 14 km. Hereafter, the simulations are referred to (as in MY13) as Δx, where x is one of the horizontal grid-spacing values. For example, grid spacing for 0.87 km is Δ0.87. In addition, we used 20,480 nodes as the maximum for conducting Δ0.87. The detailed computational performance is described in the Appendix.

The initial conditions and integration of each experiment are illustrated in Fig. 1. The initial conditions in each experiment were constructed using the results of a one-step coarser resolution after a 3 day integration, beginning 2012082200UTC, except for Δ0.87, which was initialized with the two-step coarser resolution of Δ3.5, as shown. This integration was initialized by linearly interpolated data from the final analysis of the National Center for Atmospheric Research (Kalnay et al. 1996). For example, the initial condition of Δ14 was obtained from the 3 day integration of Δ28. The simulation period was 12 h, from 2012082500UTC to 2012082512UTC. We used the data at 2012082512UTC in each experiment for the following analysis.

To define the convection in the simulation and validate such data for our analysis, we applied the following method to extract the convection in the simulated results, as in MY13. First, we defined the convective grids by optical thickness (>35) and cloud top pressure (<400 hPa) based on the cloud categorization scheme of the International Satellite Cloud Climatology Project (ISCCP) (Rossow and Schiffer 1999). Then, we could detect the convection core in the convective grids as the grid at which the vertical velocity averaged in the troposphere is greater than that in all neighboring grids. This diagnosis, using the local peak of vertical velocity, enables us to avoid the controversial discussion on the threshold dependences of detected convections. Figure 2 shows the time series of the number of convective grid points in each simulation, which was not shown in MY13. The number of convective grid points is sensitive to the initial adjustment, abruptly increasing at the beginning of the integration. A 3 day integration of the observational data seems to be long enough for the number of deep convections to become almost constant. Twelve-hour simulations initialized by the simulation results of a one-step coarser resolution are also long enough to obtain a constant number of deep

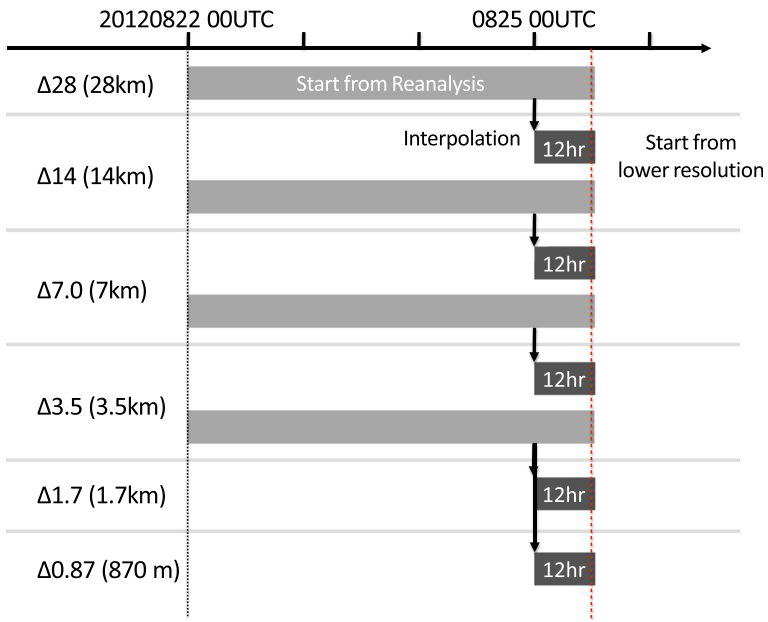

Fig. 1 Illustration of the initial condition in each experiment

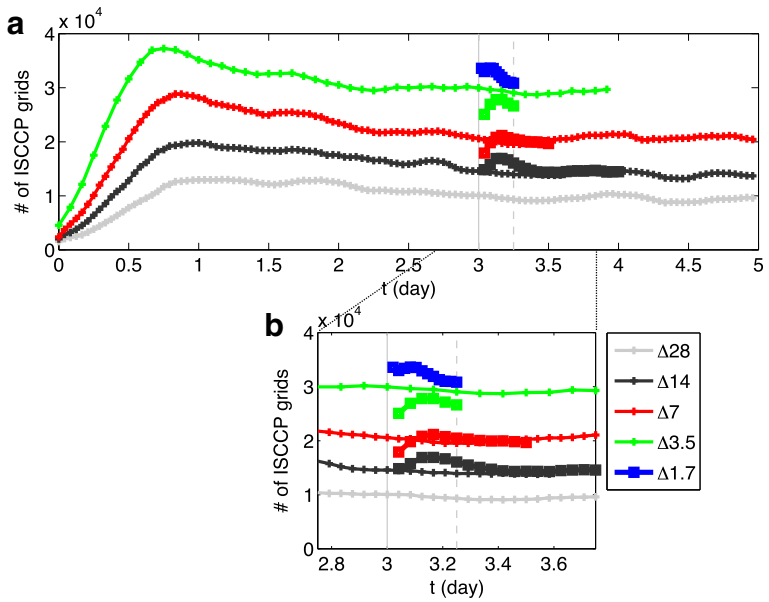

Fig. 2 **a** Time series of the convective grid numbers in each experiment. **b** Close-up view of (**a**) around 3 days

convections. Hence, the spin-up can be ignored in the data snapshot that was used.

Since we focus on the resolution dependence of the convection properties in each cloudy disturbance, we extracted the area of MJOs, TCs, mid-latitudinal low disturbances (MDL), and fronts (FRT), as in MY15. Although the method is the same as that used in MY15, we review it here to aid the following discussion. The MJO area is defined as the grid where the reconstructed OLR with first and second modes of boreal summer intraseasonal oscillation index (Kikuchi et al. 2012) was less than −10 W m^{-2}. To extract the TCs, we applied the Miyamoto et al. (2014) methodology and defined the area inside the 600 km radius from the center as the TC area. To detect the MDL centers and FRT, we first reconstructed the simulation data with coarsened 2.5° × 2.5° grid resolution. Then, we picked the MDL centers as grids at which the SLP was 5 hPa less than the areal average in the 10° radius. Finally, the MDL area was defined as inside of 1000 km from the MDL center. To extract the FRT region, we first applied the thermal frontal locator (Renard and Clarke 1965). This represented a third-order differential of the equivalent potential temperature at the 1500 m level in the horizontal direction. We detected the grid where the thermal frontal locator was >10–13 in the 2.5° × 2.5° data as a potential FRT grid. If the FRT grids lined up continuously with maximum distance greater than 10°, we defined the area as the FRT line. Finally, the FRT area was defined as the area inside the 200 km distance from the FRT line. In this study, we merge the MDL and FRT areas as the mid-latitude disturbance (MLD) area.

Figure 3 shows the horizontal distribution of the clouds in Δ14, Δ3.5, and Δ0.87, with the close-up region over the western North Pacific in the same experiment. The large-scale structure of the clouds, including cloud clusters, tropical cyclones, and mid-latitude disturbances, is almost unchanged among the grid-refinement experiments. The convection reasonably represents the global aspect in higher resolution. By comparison, among three simulations focusing on the specific area (Fig. 3d–f), it is remarkable that the Δ0.87 provides a more detailed description of the smaller-scale cloud structure. These available datasets from the grid-refinement experiments enabled us to statistically investigate the resolution dependence of the convection properties.

Results and discussion

Resolution dependence in the global field

Before we discuss the characteristics of deep convection, we need to confirm the consistency of the background environment for the simulated convections among the different grid-spacing simulations. Figure 4 shows the global mean of OLR, precipitation, zonal velocity, and vertical mass flux in all of the simulation results, with their global standard deviations. Global-mean OLR slightly increases on finer-resolution simulation. However, no meteorological variables showed significant change; they were almost constant among the different grid-spacing simulations. It is of interest that the global standard deviation of precipitation and vertical mass flux had a decreasing trend from Δ14 to Δ3.5 and that this trend is not clear in Δ1.7 and Δ0.87. On the other hand,

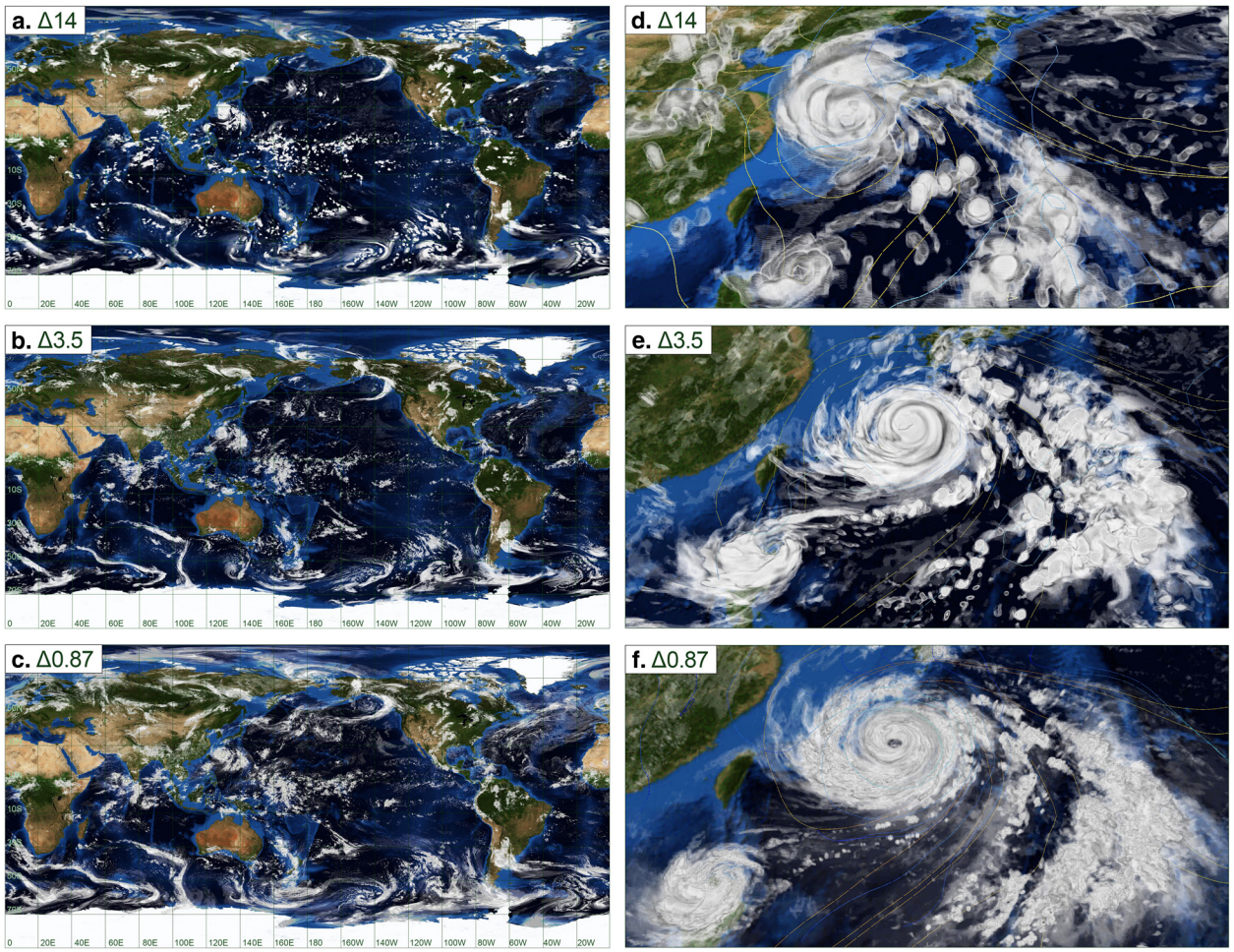

Fig. 3 Global view of cloud distribution simulated by (**a**) Δ14 km, (**b**) Δ3.5 km, and (**c**) Δ0.87 km (**d**–**f**) focusing over the western North Pacific region of (**a**–**c**)

the standard deviation of zonal wind does not show such a trend. When compared to existing observation data, the global-mean OLR in the simulations is around 240–250 W m^{-2}, which is relatively larger than the observed OLR at around 235 W m^{-2}, [obtained from daily-mean-interpolated OLR data from the National Oceanic and Atmospheric Association satellite (Liebmann and Smith 1996)]. The global-mean precipitation of around 0.15 mm h^{-1} was relatively larger than the daily-mean precipitation on August 25, 2012 [provided by the Global Precipitation Climatology Project (Adler et al. 2003) (around 0.109)]. Since these variables in Fig. 4 are based not on a specific time average but on a snapshot, slight differences are conceivable. The potential reason for no significant change is that the integration time of each simulation was 3.5 days in total, which is not enough time to respond to the interactions among different-scale atmospheric phenomena.

Figure 5 shows the zonal-mean OLR and the number of detected convections in each simulation. Zonal-mean OLR has variability among the horizontal grid spacing. This variability is large over the mid-high latitudes (especially 30 N–90 N) and small over the tropics and arid regions (30 S–10 S) in the southern hemisphere (Fig. 5a). Since we used snapshot data for this analysis, the location of the simulated convection and cloudy disturbances is different in each simulation, especially the synoptic disturbances over the mid-high latitudes, which causes the relatively large variability. Overall, zonal-mean OLR in Δ0.87 is higher than in other resolution experiments, especially over the mid-high latitudes. Zonal-mean OLR in each simulation is consistent with observation, except for the area between 30 S and 10 S. The OLR in the simulation is about 30 W m^{-2} larger than observations in the peak. This strongly affects the positive bias of the global-mean OLR in Fig. 4a.

How is the relatively larger OLR in Δ0.87 and Δ1.7 produced? MY13 pointed out that convection is resolved in simulations with finer than 2 km grid spacing. This is linked with the OLR difference. However, we also need

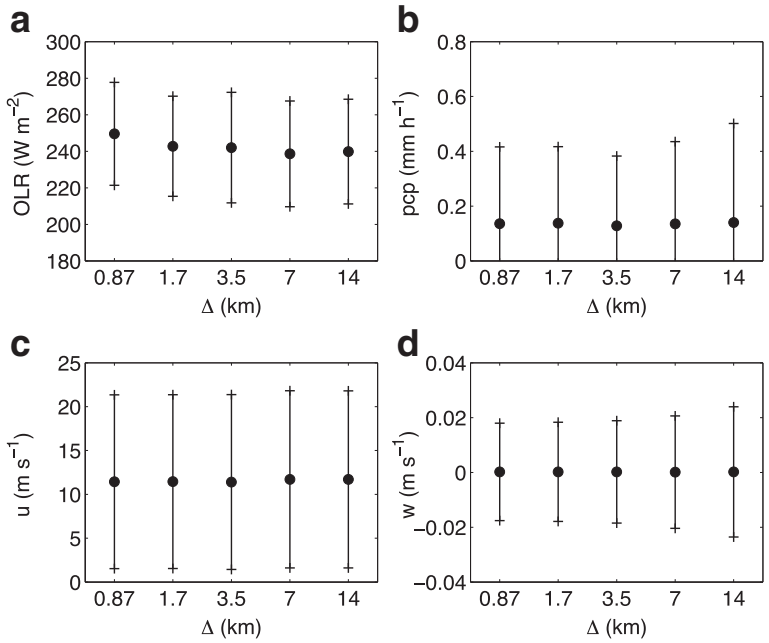

Fig. 4 Resolution dependencies of global-mean (**a**) OLR, (**b**) precipitation, (**c**) zonal wind speed at 5 km, and (**d**) vertical mass flux

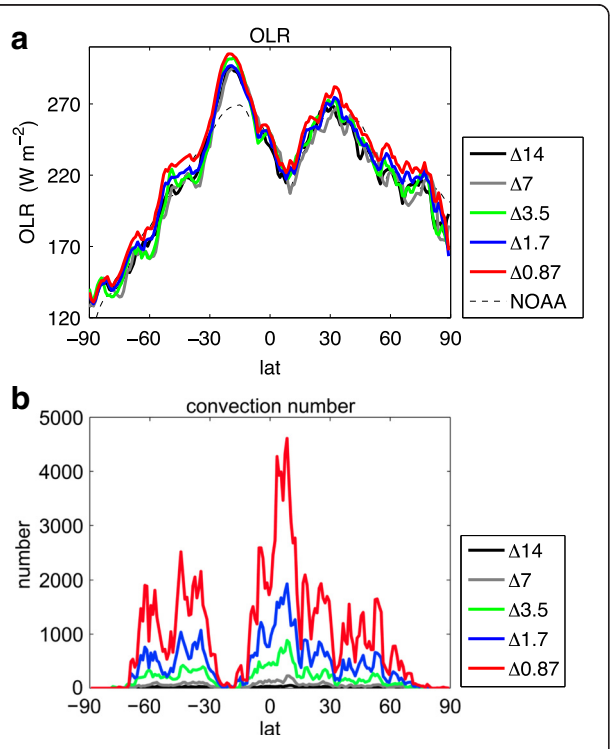

Fig. 5 Resolution dependencies of zonal-mean (**a**) OLR and (**b**) the number of detected convection cores

to investigate the resolution dependence of the other clouds in the simulation. Figure 6 shows the area of each ISCCP cloud type over the globe, defined by cloud top pressure and cloud optical thickness (Rossow and Schiffer 1999), in the grid-refinement experiments. The area of deep convection that we focused on in this study is abruptly decreased between Δ3.5 and Δ1.7, whereas the area of clear sky is increased with the same grid-spacing change. This suggests that the simulations in Δ1.7 and Δ0.87 express the proper size of the convection core with the multiple grid points and distinguish the non-cloudy sky around the convection as well. It is of interest that the areas of cirrus also increased from Δ14 and Δ0.87, implying that the simulations with higher spatial resolution are reasonably able to express the anvil associated with deep convections. According to the resolution dependence of the cloud area, increasing the zonal-mean OLR over the mid-high latitudes in the finer-resolution simulation can be explained by the increase of the area of clear sky. On the other hand, in the tropics, the zonal-mean OLR may be canceled out between the increased area of clear sky and that of cirrus with deeper convection. Further analysis is needed to quantitatively discuss the cause of resolution dependence in the other types of clouds.

The area of low cloud (e.g., stratocumulus) gradually decreases with higher resolution, especially from Δ14 and Δ3.5. Two possible reasons of this low-cloud trend are suggested. The low-cloud cells are likely to be resolved with finer resolution as well as deep convection, decreasing the low-cloud area and increasing the clear-sky area. The upward motion in the low-cloud core may

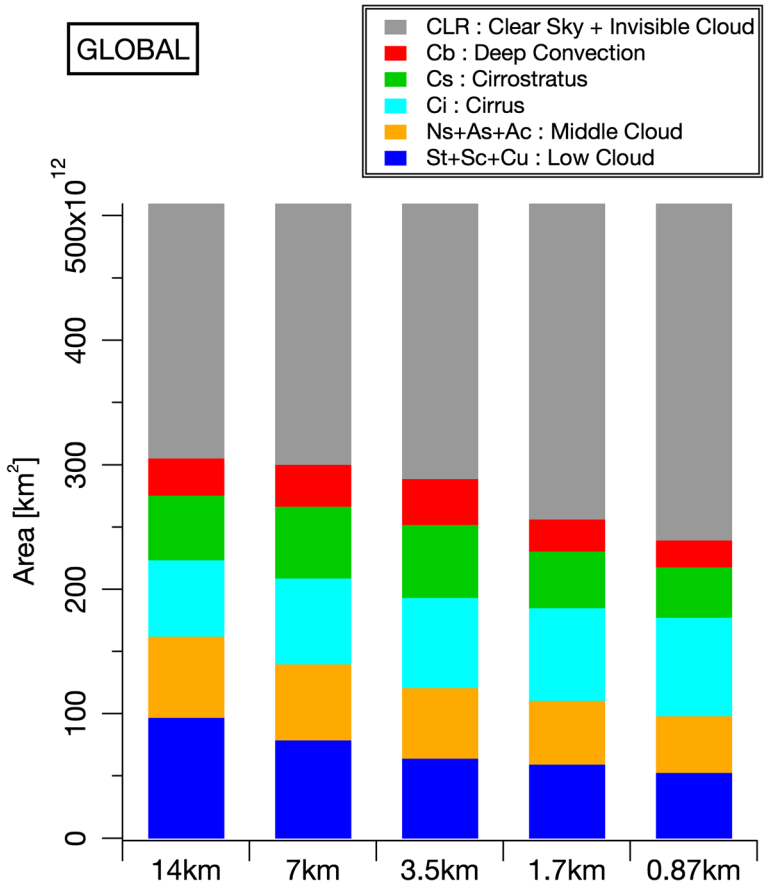

Fig. 6 Resolution dependence of total area of clear sky, deep convection, cirrostratus, cirrus, middle cloud, and low cloud, averaged over the globe

be accelerated with resolving the convection core. The faster upward motion in this model provides faster conversion from cloud to rain (Tomita 2008; Sato et al. 2015). This would reflect the decrease of the low-cloud area. On the other hand, drastically increasing the horizontal and vertical resolutions with the large-eddy simulation (LES) technique gives better representation of stratocumulus (e.g., Sato et al. 2015). Their results and our results suggest that some parameterization or tuning of microphysics is still needed in the current global modeling stage.

The area of deep convection over the globe has significantly decreased, between Δ3.5 and Δ1.7, which is consistent with the change of the convection number and the distance to the nearest convection core, as pointed out in MY13. The active convection is often accompanied by rainfall. In Fig. 7, we examine the resolution dependence of the precipitation rate at the grid of the convection core and show the frequency of the precipitation. The vertical axis denotes the logarithmic axis of the frequency. The precipitation over the convection core in Δ14, Δ7.0, and Δ3.5 is confined to less than 20 mm h^{-1}. Strong precipitation is shown in Δ1.7 (around 50 mm h^{-1}) and Δ0.87 (more than 100 mm h^{-1}). The ratio of strong precipitation, which is in excess of 20 mm h^{-1}, is drastically increased from Δ3.5 to Δ1.7. This is consistent with the idea that convection is resolved using multiple grid points in simulations and enhancement of the upward motion with the grid

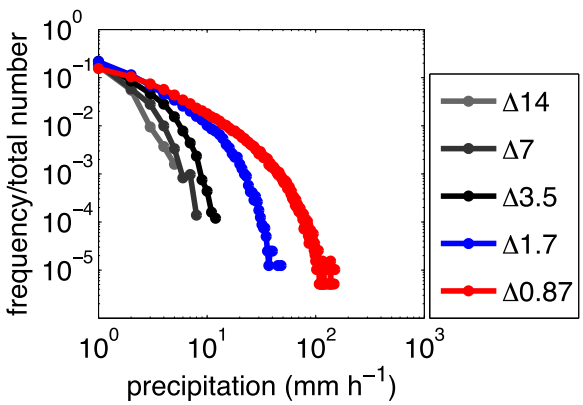

Fig. 7 Probability function of precipitation at the grid of the simulated convection core at each horizontal resolution

spacing of less than 2 km. The global-mean precipitation is almost constant in the different grid-spacing simulations. In the case of grid spacing of more than 2 km, convection with rainfall is described as one grid for the larger area, and then, the rainfall intensity is relatively weak. In contrast, in the case of grid spacing of less than 2 km, the enhancement of the upward motion provides strong precipitation at the convection core grid. In addition, we suggest the two effects of (1) resolving the convection with multiple grid points and (2) enhancement of the convection activity over the tropics. Since the former induce the increasing of the area of clear sky and OLR and the latter induce the decrease of OLR, the OLR over the tropics tends to be less variable among the simulations due to the balance of the two effects (Fig. 5a). We also speculated that the decreasing trend in the standard deviation of global-mean precipitation between Δ14 and Δ3.5 is linked to the decrease of total cloud area and the increase of the sample grid number, whereas this trend would be canceled out by the increasing heavy rainfall in Δ1.7 and Δ0.87.

In short, we confirm the diversity of the resolution dependence of OLR in the latitude and area of each cloud type among the grid-refinement simulations, although the global mean is consistent among the simulations. We also found that the convection resolved by multiple grid points in Δ1.7 and Δ0.87 was accompanied by stronger rainfall.

Resolution dependence on convection properties

First, we briefly introduce the results in MY13 and describe the resolution dependence of the simulated convection properties averaging over the globe. MY13 found that the convection core is resolved with multiple grid points when the horizontal grid space is less than 2 km. Figure 8 shows the resolution dependence of (a) the number of convections and (b) grid distance to the nearest convection core over the globe. The number of convection core in Δ3.5 and Δ7.0 is about four times larger than the number in Δ7.0 and Δ14; hence, those are shown on the $\log\Delta^4$ line starting from the number in Δ14 (dashed line in Fig. 8a). This indicates that the simulated convection in double resolution is simply an interpolated result of the original. However, the rate of increase in the number of convection core is decreased from Δ3.5 to Δ1.7. In other words, the number tends to distance from the $\log\Delta^4$ line in Δ1.7. If the number of the simulated convection core reaches the appropriate value, it is constant regardless of the grid spacing. Clear convergence was not confirmed even in Δ0.87; however, the increase rate of the convection is changed between the grid spacing of 3.5 and 1.7 km.

The resolution dependence in the histogram of the minimum distance between convection cores is also changed between Δ3.5 and Δ1.7 (Fig. 8b). The peak of frequency in Δ14, Δ7.0, and Δ3.5 appears in four grind points, whereas that in Δ1.7 and Δ0.87 is larger than four. Since the actual length of four grid points is different in each experiment, we suggest that the simulated convection distance in coarser resolution experiments is determined not physically but numerically; it may depend on the numerical discretization method. Hence, we speculated that the realistic distance between convection cores appears to be larger than the effective resolution in Δ1.7 and Δ0.87.

To investigate the horizontal diversity of the above features as a global mean, we have further analyzed the resolution dependence of the simulated convection properties, considering the perspective of the land-ocean difference (4.1), the latitude difference (4.2), and the

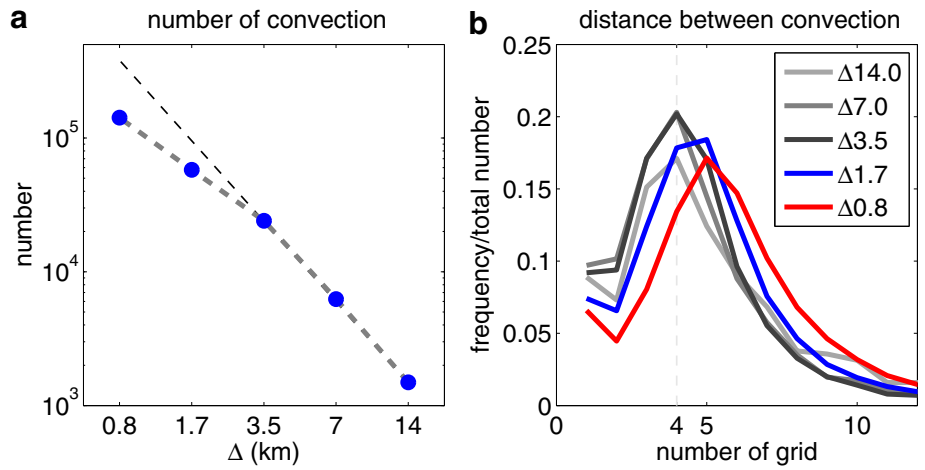

Fig. 8 Resolution dependencies of convective features: **a** the number of convections and (**b**) grid distance to the nearest convective feature. The *thin dashed line* in (**a**) indicates a log Δ^4 crossing at the point of Δ14 as a reference (Miyamoto et al 2013)

difference in cloudy disturbances (4.3), and we picked up the convections over the other specific region (4.4) in the following sections.

Land and ocean difference

Different surface conditions are one of the potential factors for characterizing convection. We investigated convection properties over land and ocean separately. Figure 9 shows the number of convections and grid distance to the nearest convection core in each experiment as similar as Fig. 8 with vertical velocity of composited convections based on the detected convection cores in Δ0.87 over land and ocean, respectively. The number of convections over ocean is larger than those over land because many deep convection cores are found over the tropical ocean. The number of convections drastically changes between Δ3.5 and Δ1.7, over both land and ocean. The grid distance between convections also changes at around the 2 km grid spacing; the peak of frequency tends to be larger from four grids. This is consistent with the global mean (Fig. 8). The vertical velocity of the convection core is slightly larger in the convection over land than that over ocean. In addition, a decrease of the increasing rate of the convection number occurred in the simulation of Δ3.5 over land. However, both convection properties over land and ocean are very consistent with the global-mean feature (Fig. 8), and in a qualitative sense, little significant difference in the convection feature over land and over ocean is found in this study.

Latitudinal difference

The location of the convection, especially in latitude, should be connected to the thermal condition affecting the property of convection. To examine the latitude difference of convection properties and its resolution dependence, we divided the convection over the globe into four groups based on the gaps in its zonal-mean distribution (Fig. 5): (1) 70 S–30 S, (2) 15 S–15 N, (3) 15 N–30 N, and (4) 30 N–70 N. Figure 10 shows the change in the number of detected convections and grid distance to the nearest convection core with the horizontal grid space in each region. Significant difference between the tropics and the mid-latitude region is found. The increasing rate of the convection number in the mid-latitude begins to decrease between Δ3.5 and Δ1.7.

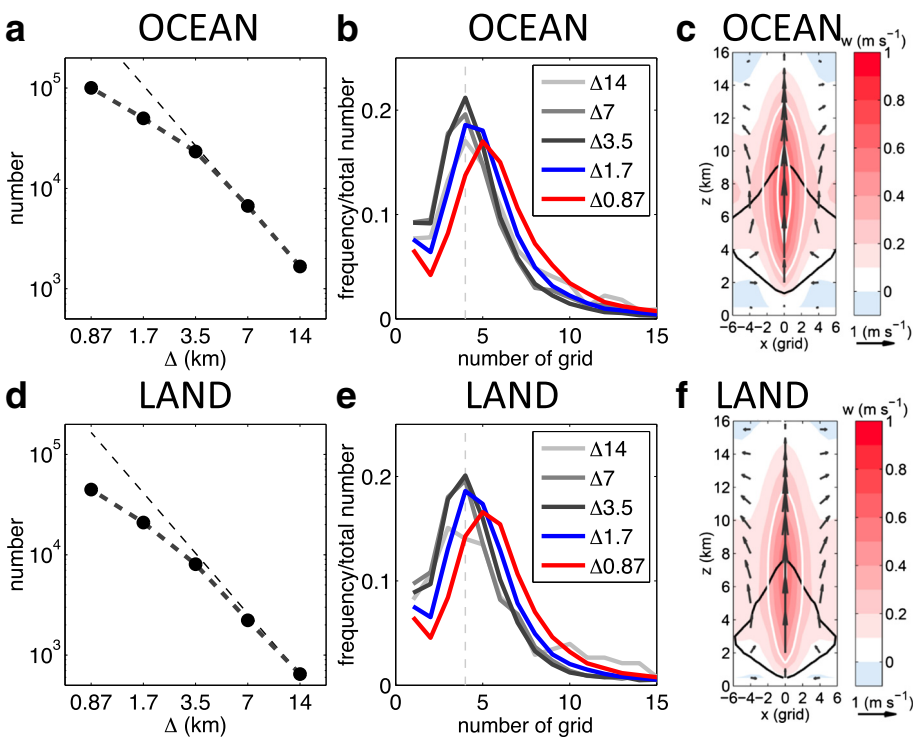

Fig. 9 Resolution dependence of (**a**) the number of convections and (**b**) grid distance to the nearest convection core detected over land. The *thin dashed line* in (**a**) denotes a log Δ^4 based on the value of Δ14 as a reference. **c** Radius-height cross section for composites of vertical velocity (w: *shaded*) and velocity vector of radial and vertical velocity (vector) for the simulated convection core detected over ocean in Δ0.87. The *white contour* denotes 0.3 and 0.6 ms^{-1}, and the *black contour* indicates the mixing ratio of hydrometeors weighted by air density with an interval of 0.5 g m^{-3}. **d**–**f** The same as (**a**–**c**) but for the convection detected over land

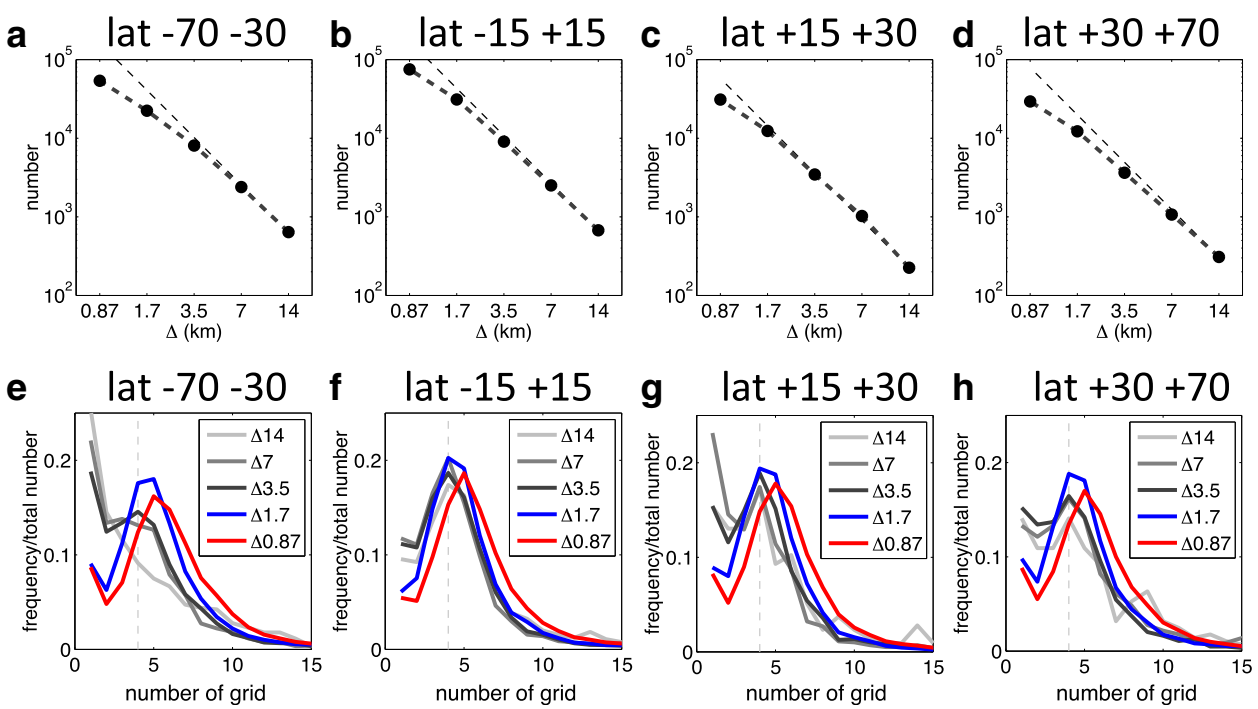

Fig. 10 Resolution dependence of (**a**) the number of convections and (**e**) grid distance to the nearest convection core detected over the latitudinal area between 70 S and 30 S. Figure structure is the same as Fig. 8. The same as (**a**) and (**e**) but for the area between 15 S and 15 N (**b**, **f**); 15 N and 30 N (**c**, **g**); and 30 N and 70 N (**d**, **h**)

On the other hand, the convection number over the tropics tends to converge between Δ0.87 and Δ1.7.

The grid distance between convection cores also shows the difference between the mid-latitude and the tropics. The distance of the mid-latitude convection becomes larger than four grids in Δ1.7 and Δ0.87. Interestingly, the distance to the mid-latitude convection in the coarse resolution has another peak around one grid. This indicates the convections occur close to one another. When the convection core is resolved with multiple grid points in Δ1.7 and Δ0.87, the number of convections with one grid distance is dramatically decreased and the number of convections with larger grid distance is increased as well. This also supports that convections in the mid-latitudes are resolved and have a realistic distance to the nearest convection cores in the simulation of less than 2 km. In contrast, the grid distance between convections over the tropics is distributed widely, with the peak at four to five grids. Since the increasing ratio of the convection number does not change significantly around Δ1.7 and Δ3.5, the grid distance also does not change drastically. However, the distance becomes larger than four grid points in Δ0.87. Meanwhile, the change of grid distance between convection cores can be seen from Δ1.7 to Δ0.87 in the whole area. It also supports that most of the convections would be resolved with multiple grid points in Δ0.87. In short, the resolution dependence of the convection shows different trends in the tropics and the mid-latitude area.

Different cloudy disturbances

MY15 showed the diversity of convection properties in various disturbances in Δ0.87. In this study, we investigated the resolution dependence of the convection number in cloudy disturbances: MJO, TC, and mid-latitude disturbances, as in MY15. Each disturbance region is shown in Fig. 11. In this study, we also add the category of "other," which is defined as all convections that are not located in any of the above cloudy disturbances. Figure 12 shows the resolution dependence of the number of detected convections in each cloudy disturbance, "other," and global accumulation. The global accumulation is the same as in Fig. 8. The trend of the number of convections does not converge at about 2 km except for the convections categorized as "other" in this study. The number of convections in each cloudy disturbance in Δ0.87 is about 10^4, while those categorized as "other" is about 10^5, which is similar to the global accumulation. Therefore, the convection categorized as "other" makes a large contribution to the global aspects, while the contribution of the convection in the cloudy disturbance to the global aspect is limited. The difference in the convection numbers between global accumulation and each cloudy disturbance clearly shows that the convergent trend is weaker in MJO and TC. This would affect the latitudinal difference in the "Latitudinal difference" section. It is important that the trend of the convection

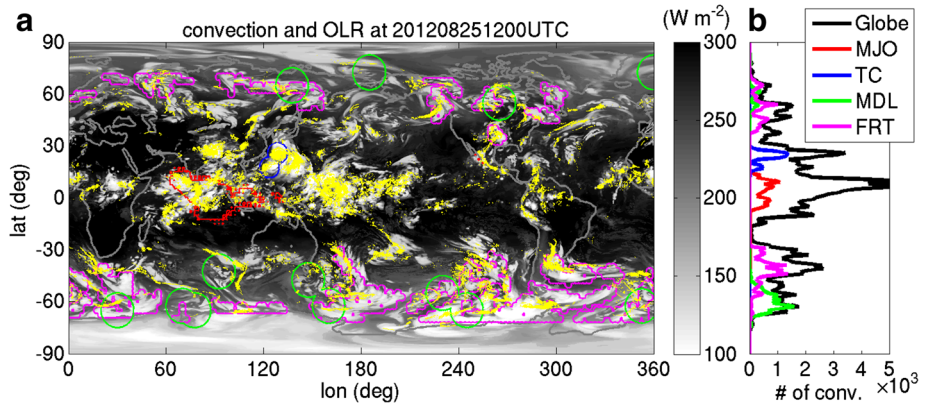

Fig. 11 **a** Horizontal distribution of the extracted convection core in Δ0.87 (*yellow*) and the defined area of MJO (*red*), TC (*blue*), MDL (*green*), and FRT (*magenta*) disturbances, respectively. **b** Latitudinal profile of the number of the extracted convective grid points in each disturbance in Δ0.87 (Miyamoto et al., 2015)

number in the organized cloudy disturbance has less convergence around 2 km but tends to converge from Δ1.7 to Δ0.87 at least. This supports that most of the organized convection in the tropics would be resolved in Δ0.87.

Specific area

We also checked the convection properties and resolution dependence in the specific area where the convection is active. We selected the three regions: (1) mid-Pacific (150 E–150 W, 15 S–15 N), (2) Maritime Continent (90 E–150 E, 15 S–10 N), and (3) Tibetan Plateau (70 E–100 E, 20 N–35 N), based on the lower OLR in the surrounding areas and the large number of detected convections (about 10^4) (see Fig. 11). These three areas can be categorized as the tropics or Asian monsoon region. The essential change of the convection properties starts between Δ1.7 and Δ0.87 over the mid-Pacific and Maritime Continent

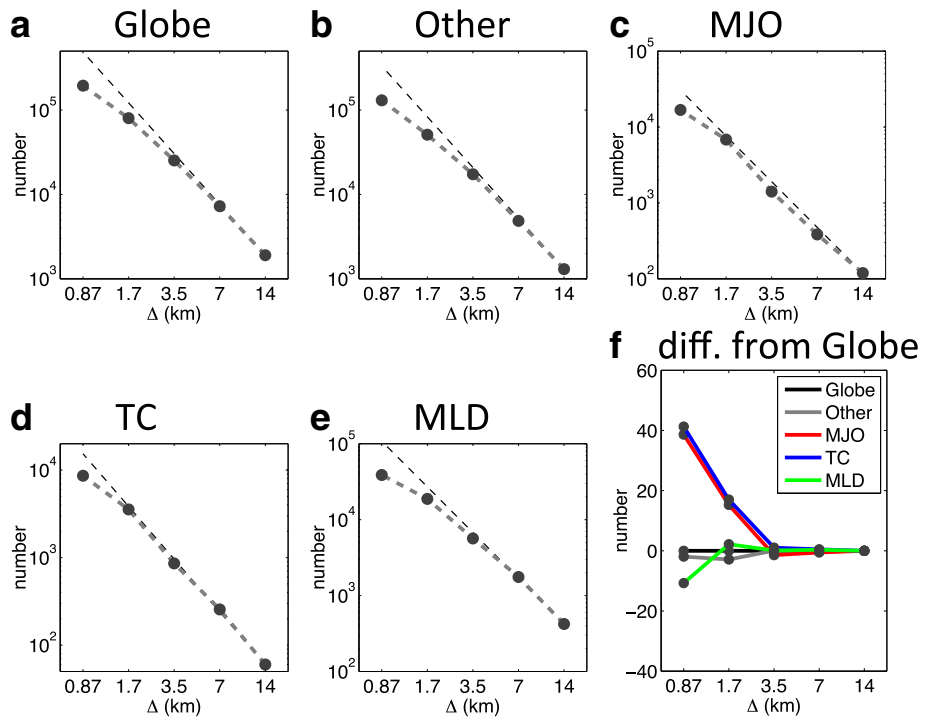

Fig. 12 Resolution dependence of the number of detected convections in (**a**) the globe, (**b**) other, (**c**) MJO, (**d**) TC, (**e**) MLD (MDL and FRT), and (**f**) difference from globe after notarizing based on the convection number of Δ14 in each disturbance. The *thin dashed line* in (**a**–**e**) denotes a log Δ^4 based on the value of each Δ14 as a reference

(Fig. 13). The number of the convection distances around one to two grids is also drastically decreased between Δ3.5 and Δ1.7. On the other hand, the convections over the Tibetan Plateau do not show a significant convergent trend for the number of convections. Since the convections over the Tibetan Plateau and mid-Pacific seem to be in the organized cloud system (Fig. 11), it is implied that convections forced by large-scale disturbances tend to have a less significant change of properties, even in Δ1.7. Although the detailed cloud system over the mid-Pacific and Tibetan Plateau is not determined in this study, environmental conditions over those areas should be explained for a better understanding of the resolution dependence of the convection.

Conclusions

We comprehensively investigated the simulated convection properties and global-mean field by focusing on their resolution dependence, based on grid-refinement experiments from 14 to 0.87 km grid spacing by using NICAM. The convergence trend for the number of convections is confirmed to occur between Δ3.5 and Δ1.7 (Miyamoto et al. 2013). The global mean of vertical mass flux, precipitation, and zonal wind at 5 km are conserved in different resolution simulations (Fig. 4). Global-mean OLR is slightly increased in Δ1.7 and Δ0.87, and this trend is more remarkable over the mid-latitude area (Fig. 5). Global-mean precipitation has no resolution dependence, while the precipitation intensity associated with deep convection becomes higher in increasing resolutions (Fig. 7). Interestingly, the ratio of the cloud type over the globe is different between simulations. The area of low and middle clouds is also decreased with increasing the resolution as well as deep convection, and those of clear sky are increased particularly in Δ1.7 and Δ0.87 (Fig. 6). These differences reflect the resolution dependence of zonal-mean OLR (Fig. 5).

MY13 pointed out that the essential change of the number of convection cores and distance to the nearest convective core occurred around the 2 km grid spacing as a global mean (Fig. 8). We further investigated the resolution dependence of the simulated convection from the wider and more various perspectives than MY13. We found that the results in MY13 were different between latitudinal regions and cloudy disturbances (Figs. 10 and 12), although the trend of the convection number and grid distance between convection cores is not significantly different between over land and ocean (Fig. 9). The convergence trend for the number of convections in the mid-latitude area is more predominant than that in the tropics (Fig. 10). The essential change of the convection properties around the 2 km grid spacing is not clear, even in Δ1.7, for the convections in the cloudy disturbances categorized by MY15. In contrast, the convection properties that are not detected in the categorized cloudy disturbance change drastically between Δ3.5 and Δ1.7, which is similar to global accumulations (Fig. 12). Moreover, the convections in the cloud cluster over the mid-Pacific and Maritime Continent show a similar trend of convections in MJO and TC (Fig. 13).

In this study, we showed the diversity of the resolution dependency of the simulated convection properties.

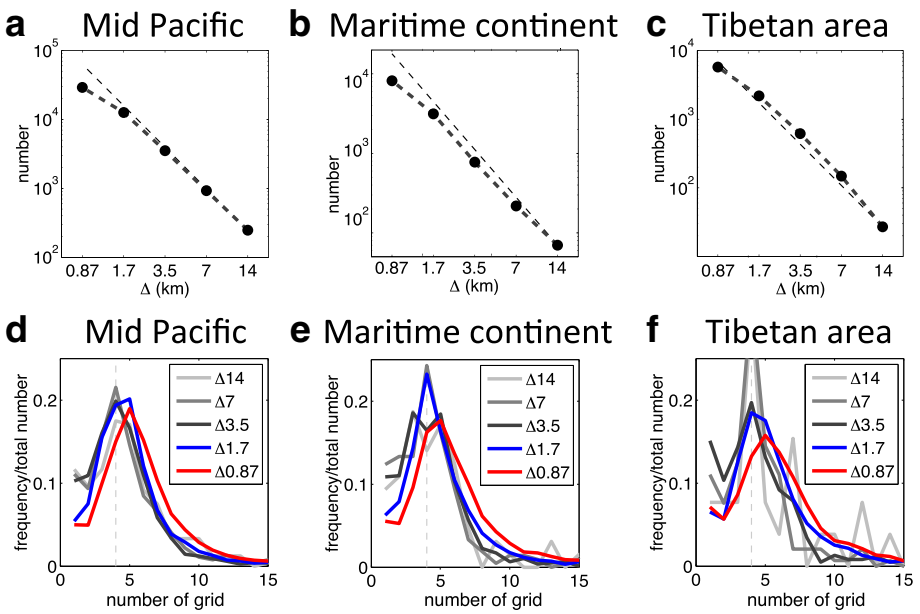

Fig. 13 Resolution dependence of (**a**) the number of convections over the mid-Pacific. **b** The same as (**a**) but for over the Maritime Continent. **c** The same as (**a**) but for over the Tibetan area. **d**–**f** Grid distance to the nearest convection core detected. The same area as (**a**–**c**)

Convections over the mid-latitudes and convections detected other than in the cloudy disturbances show the essential change of properties more clearly around the 2 km grid spacing, largely contributing the global mean. We speculate that this difference is related to the strength of forcing under the tropical cloudy disturbance. In fact, larger CAPE in the MJO area and larger low-level convergence in the TC area are confirmed in MY15. It is also speculated that the convection naturally arises as many as possible in such area under the strong forcing. Therefore, the convections are tightly packed in the cloudy disturbance, the size of convection core is relatively smaller than other categorized convections, and the convection core is not resolved by multiple grid points, even in Δ1.7. In contrast, where the environmental atmosphere allows convection to occur freely, the simulated convection, likely the isolated convective cloud, is relatively larger than that in tropical cloudy disturbances and it can be resolved by multiple grid points in Δ1.7 and Δ0.87. Since this difference in the relationship between cloudy disturbances appears to not link with the surface condition, it does not affect the convection property difference between convection over land and ocean.

We found a difference in resolution dependency in the simulated convection property. It is important that the convections, even in cloudy disturbances, show a convergent trend for the number and are resolved not by a single grid but by multiple grid points between Δ1.7 and Δ0.87, at least, despite the existence of the above difference. This is a noteworthy aspect for a series of grid-refinement experiments. It recalls the further high spatial resolution for better simulations of tropical convections. This would bring a better understanding of tropical cloudy disturbances, based on the hierarchical structure of convections. Hence, longer time integration of the global atmosphere in the 0.87 km grid spacing in the future will provide significant discussion about the interaction between convections and cloudy disturbances.

Appendix

In the highest resolution run of Δ0.87, we achieved the greatest computational performance for weak scaling on the K computer. Figure 14 from Terai et al. (2014) shows a computational performance and scalability of NICAM on the K computer. At this scaling test, we increased the number of grids while increasing the number of nodes. We achieved 10 % of the peak performance using five nodes (40 cores) with 56 km of horizontal grid spacing. The performance was maintained to 8 % with 81,920 nodes (655,360 cores) and 0.44 km of horizontal grid spacing. Elapsed time per step was increased ~15 % from 80 nodes (Δ14 run) to 20,480 nodes (Δ0.87 run) due to the imbalance of the number of computations. This load imbalance is mainly related to computation in cloud microphysics and the spatial inhomogeneity of cloud distribution. In this study, the run of Δ0.87 with 20,480 nodes was conducted as the highest resolution of the production run, by taking the total computational time and resources into account.

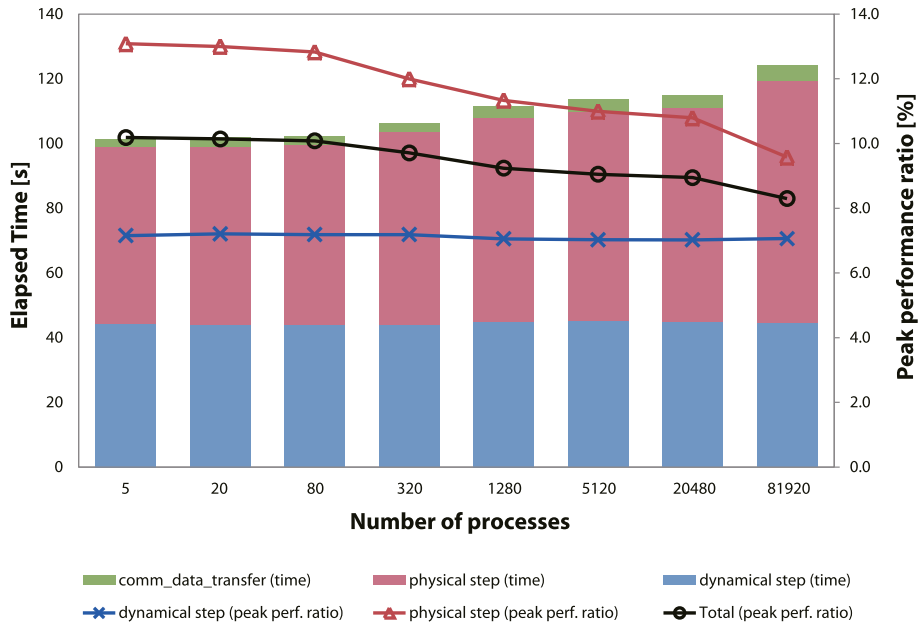

Fig. 14 Elapsed time and peak performance ratio in weak scaling (Terai et al. 2014)

Acknowledgements
The authors are grateful to the editor of the Progress in Earth and Planetary Science and anonymous reviewers. Special thanks are due to Drs. S. Nishizawa Y. Sato, and S. Iga in the RIKEN Advanced Institute for Computer Science (AICS) for the valuable comments. The simulations were performed using the K computer at the RIKEN AICS under the supported by Strategic Programs for Innovative Research (SPIRE) Field 3 (Projection of Planet Earth Variations for Mitigating Natural Disasters).

Authors' contributions
YK conceived the idea, organized this study, and wrote the manuscript. YM carried out the simulations, analyzed the simulated results, and collaborated with YK to draft the manuscript. RY and TY supported to conduct the simulation and analysis with arranging the necessary environment on the K computer. HY led the implementation of NICAM on the K computer. HT coordinated the project and collaborated with YK in the construction of the manuscript. All co-authors provided guidance for the analysis and commented on the manuscript. All authors read and approved the final manuscript.

Competing interests
The authors declare that they have no competing interests.

Author details
[1]RIKEN Advanced Institute for Computational Science, 7-1-26 Minatojima-minami-machi, Chuo-ku, Kobe, Hyogo 650-0047, Japan. [2]Japan Agency for Marine-Earth Science and Technology, 2-15, Natsushima-cho, Yokosuka, Kanagawa 237-0061, Japan.

Received: 3 December 2015 Accepted: 11 May 2016
Published online: 06 June 2016

References

Adler RF et al (2003) The version-2 global precipitation climatology project (GPCP) monthly precipitation analysis (1979-present). J Hydrometeorol 4:1147–1167
Arakawa A, Schubert WH (1974) Interaction of a cumulus cloud ensemble with large-scale environment. Part 1. J Atmos Sci 31:674–701
Emanuel KA, Raymond DJ (1993) The Representation of cumulus convection in numerical modelsAmerican Meteorological Society, Boston, Mass, p 246
Fudeyasu H, Wang YQ, Satoh M, Nasuno T, Miura H, Yanase W (2008) Global cloud-system-resolving model NICAM successfully simulated the lifecycles of two real tropical cyclones. Geophys Res Lett 35: doi: 10.1029/2008gl036003.
Gill AE, (1982) Atmosphere-ocean dynamics. Academic Press, New York, p 662
Kain JS, Fritsch JM (1990) A one-dimensional entraining/detraining plume model and its application in convective parameterization. J Atmos Sci 47:2784–2802
Kajikawa Y, Yamaura T, Tomita H, Satoh M (2015) Impact of tropical disturbance on the Indian summer monsoon onset simulated by a global cloud-system-resolving model. SOLA 11:80–84. doi:10.2151/sola.2015-020
Kalnay E et al (1996) The NCEP/NCAR 40-year reanalysis project. Bull Amer Meteorol Soc 77:437–471
Kikuchi K, Wang B, Kajikawa Y (2012) Bimodal representation of the tropical intraseasonal oscillation. Clim Dynam 38:1989–2000. doi:10.1007/s00382-011-1159-1
Kodama C et al (2015) A 20-year climatology of a NICAM AMIP-type simulation. J Meteorol Soc Jpn 93:393–424. doi:10.2151/jmsj.2015-024
Liebmann B, Smith CA (1996) Description of a complete (interpolated) outgoing longwave radiation dataset. Bull Amer Meteorol Soc 77:1275–1277
Louis JF (1979) A parametric model of vertical eddy fluxes in the atmosphere. Bound-Lay Meteorol 17:187–202
Mapes BE, Houze RA (1993) Cloud clusters and superclusters over the oceanic warm pool. Mon Weather Rev 121:1398–1415
Miura H, Satoh M, Nasuno T, Noda AT, Oouchi K (2007) A Madden-Julian oscillation event realistically simulated by a global cloud-resolving model. Science 318:1763–1765. doi:10.1126/science.1148443
Miyakawa, T., and Coauthors (2014) Madden-Julian oscillation prediction skill of a new-generation global model demonstrated using a supercomputer. Nat Commun 5, doi: 10.1038/Ncomms4769
Miyamoto Y, Kajikawa Y, Yoshida R, Yamaura T, Yashiro H, Tomita H (2013) Deep moist atmospheric convection in a subkilometer global simulation. Geophys Res Lett 40:4922–4926. doi:10.1002/Grl.50944
Miyamoto Y, Satoh M, Tomita H, Oouchi K, Yamada Y, Kodama C, Kinter J (2014) Gradient wind balance in tropical cyclones in high-resolution global experiments. Mon Weather Rev 142:1908–1926. doi:10.1175/Mwr-D-13-00115.1
Miyamoto Y, Yoshida R, Yamaura T, Yashiro H, Tomita H, Kajikawa Y (2015) Does convection vary in different cloud disturbances? Atmos Sci Lett 16:305–309
Mizuta R et al (2006) 20-km-mesh global climate simulations using JMA-GSM model—mean climate states. J Meteorol Soc Jpn 84:165–185
Mrowiec AA, and Coauthors (2012) Analysis of cloud-resolving simulations of a tropical mesoscale convective system observed during TWP-ICE: vertical fluxes and draft properties in convective and stratiform regions. J Geophys Res-Atmos 117 doi: 10.1029/2012jd017759
Nakano M, M Sawada, T Nasuno, M Satoh (2015) Intraseasonal variability and tropical cyclogenesis in the western North Pacific simulated by a global nonhydrostatic atmospheric model, 2014GL062479, 10.1002/2014gl062479
Nakazawa T (1988) Tropical super clusters within intraseasonal variations over the western Pacific. J Meteorol Soc Jpn 66:823–839
Noda AT, Oouchi K, Satoh M, Tomita H, Iga S, Tsushima Y (2010) Importance of the subgrid-scale turbulent moist process: cloud distribution in global cloud-resolving simulations. Atmos Res 96:208–217
Randall D, Khairoutdinov M, Arakawa A, Grabowski W (2003) Breaking the cloud parameterization deadlock. Bull Amer Meteorol Soc 84:1547–1564. doi:10.1175/Bams-84-11-1547
Renard RJ, Clarke LC (1965) Experiments in numerical objective frontal analysis. Mon Weather Rev 93:547–556
Rossow WB, Schiffer RA (1999) Advances in understanding clouds from ISCCP. Bull Amer Meteorol Soc 80:2261–2287
Saito K et al (2006) The operational JMA nonhydrostatic mesoscale model. Mon Weather Rev 134:1266–1298
Sato Y, S Nishizawa, H Yashiro, Y Miyamoto, Y Kajikawa, H Tomita (2015) Component-level intercomparison: proof of concept using the case of shallow cumulus simulation, 2, 10.1186/s40645-015-0053-6.
Satoh, M., and Coauthors (2014) The non-hydrostatic icosahedral atmospheric model: description and development., 1, doi:10.1186/s40645-014-0018-1
Satoh M, Matsuno T, Tomita H, Miura H, Nasuno T, Iga S (2008) Nonhydrostatic icosahedral atmospheric model (NICAM) for global cloud resolving simulations. J Comput Phys 227:3486–3514. doi:10.1016/j.jcp.2007.02.006
Sekiguchi M, Nakajima T (2008) A k-distribution-based radiation code and its computational optimization for an atmospheric general circulation model. J Quant Spectrosc Radiat Trans 109:2779–2793
Simmons AJ, Burridge DM, Jarraud M, Girard C, Wergen W (1989) The ECMWF medium-range prediction models development of the numerical formulations and the impact of increased resolution. Meteorol Atmos Phys 40:28–60
Stephens GL et al (2010) Dreary state of precipitation in global models. J J Geophys Res-Atmos 115:D24211. doi:10.1029/2010JD014532
Stevens B, Bony S (2013) What are climate models missing? Science 340:1053–1054. doi:10.1126/science.1237554
Terai M, H Yashiro, K Sakamoto, S Iga, H Tomita, M Satoh, K Minami (2014) Performance optimization and evaluation of a global climate application using a 440m horizontal mesh on the K computer., Abstract from International Conference for High Performance Computing, Networking, Storage and Analysis, SC14, New Orleans, United States
Tomita H (2008) New microphysical schemes with five and six categories by diagnostic generation of cloud ice. J Meteorol Soc Jpn 86a: 121-142
Tomita H, Satoh M (2004) A new dynamical framework of nonhydrostatic global model using the icosahedral grid. Fluid Dyn Res 34:357–400. doi:10.1016/j.fluiddyn.2004.03.003
Webster PJ (1972) Response of tropical atmosphere to local, steady forcing. Mon Weather Re 100:518
Yamaura T, Kajikawa Y, Tomita H, Satoh M (2013) Possible impact of a tropical cyclone on the northward migration of the Baiu frontal zone. SOLA 9:89–93. doi:10.2151/sola.2013-020
Yoshimura H, Mizuta R, Murakami H (2015) A spectral cumulus parameterization scheme interpolating between two convective updrafts with semi-lagrangian calculation of transport by compensatory subsidence. Mon Weather Rev 143:597–621. doi:10.1175/Mwr-D-14-00068.1